Deformation of Diopside Single Crystal at Mantle Pressure, 1: Mechanical data

Elodie Amiguet, Paul Raterron, Patrick Cordier, Hélène Couvy, Jiuhua Chen

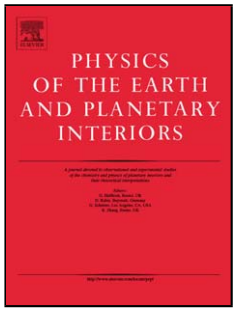

Title: Deformation of Diopside Single Crystal at Mantle Pressure, 1: Mechanical data

Authors: Elodie Amiguet, Paul Raterron, Patrick Cordier, Hélène Couvy, Jiuhua Chen

PII: S0031-9201(09)00171-X
DOI: doi:10.1016/j.pepi.2009.08.010
Reference: PEPI 5192

To appear in: *Physics of the Earth and Planetary Interiors*

Received date: 10-3-2009
Revised date: 3-7-2009
Accepted date: 12-8-2009

Please cite this article as: Amiguet, E., Raterron, P., Cordier, P., Couvy, H., Chen, J., Deformation of Diopside Single Crystal at Mantle Pressure, 1: Mechanical data, *Physics of the Earth and Planetary Interiors* (2008), doi:10.1016/j.pepi.2009.08.010

Revised Manuscript

Deformation of Diopside Single Crystal at Mantle Pressure, 1: Mechanical data

Elodie Amiguet[1], Paul Raterron[1*], Patrick Cordier[1], Hélène Couvy[2], Jiuhua Chen[2]

[1] Laboratoire de Structure et Propriétés de l'Etat Solide, CNRS 8008, Université des Sciences et Technologies de Lille, F-59655 Villeneuve d'Ascq Cedex, France

[2] The CeSMEC, Florida International University, University Park Campus, Blg. VH140, Miami, Florida 33199, USA

* Corresponding author: Paul.Raterron@univ-lille1.fr ; Tel.: +33 320 43 4686; Fax: 6591

Abstract

Steady state deformation experiments were carried out in a Deformation-DIA high-pressure apparatus (D-DIA) on oriented diopside single crystals, at pressure (P) ranging from 3.8 to 8.8 GPa, temperature (T) from 1100° to 1400°C, and differential stress (σ) between 0.2 and 1.7 GPa. Three compression directions were chosen in order to test the activity of diopside dislocation slip systems, i.e., ½<110>$\{1\bar{1}0\}$ systems activated together, both [100](010) and [010](100) systems together, or [001] dislocation slip activated in (100), (010) and {110} planes. Constant applied stress and specimen strain rates ($\dot{\varepsilon}$) were monitored *in situ* using time-resolved synchrotron X-ray diffraction and radiography, respectively. Transmission electron microscopy (TEM) investigation of the run products revealed that dislocation creep was responsible for sample deformation. Comparison of the present high-P data with those obtained at room-P by Raterron and Jaoul (1991) - on similar crystals deformed at comparable T-σ conditions - allows quantifying the effect of P on ½<110>$\{1\bar{1}0\}$ activity. This translates into the activation volume $V^* = 17 \pm 6$ cm^3/mol in the corresponding creep power law. Our data also show that both ½<110> dislocation slips and [001] have comparable slip activities at mantle P and T, while [100](010) and [010](100) slip systems remain marginal. These results show that P has a significant effect on high-T dislocation creep in diopside, the higher the pressure the harder the crystal, and that this effect is stronger on ½<110> slip than on [001] slip.

Keywords: upper mantle, clinopyroxenes, diopside, high pressure, dislocation creep, slip systems, rheological law, activation volume

1. Introduction

Clinopyroxenes (cpx) are major constituents of eclogites, and are present in excess of 10 vol.% at most depths in the pyrolitic upper mantle (Green et Ringwood, 1963). Among mantle minerals, they exhibit the strongest anisotropy for seismic wave propagation (see Mainprice et al., 2000). Cpx plastic properties may thus significantly affect both mantle rheology and seismic anisotropy. Yet, no study of cpx rheology at high-pressure (typically $P > 3$ GPa) has been reported so far - mostly because of technical limitations - whereas P reaches 14 GPa in the deep upper mantle at the transition zone boundary. A number of experimental studies of cpx crystal and/or cpx-rich aggregate deformation, carried out at low $P \leq 3$ GPa in dead load apparatuses, Paterson machines, and Griggs apparati, have been reported since Griggs et al.'s (1960) early work (Raleigh and Talbot, 1967; Avé Lallemant 1978; Kollé and Blacic, 1982, 1983; Kirby and Kronenberg, 1984; Boland and Tullis, 1986; Raterron et Jaoul, 1991; Ingrin et al., 1991; Ingrin et al., 1992; Jaoul et Raterron, 1994; Raterron et al., 1994; Mauler et al., 2000; Bystricky and Mackwell, 2001; Dimanov et al., 2003; Chen et al., 2006; Zhang et al., 2006; Zhang and Green, 2007). These studies address the fundamentals of cpx plastic deformation mechanisms and their respective activities as a function of temperature (T) and fluid (i.e., water, oxygen) fugacities, in a pressure range representative of the Earth crust and uppermost mantle of the lithosphere. .

We report here the first investigation of cpx rheology at asthenosphere pressure. We investigate the high-temperature ($T \geq 1100$°C) plasticity of diopside single crystals because i) diopside is a good representative of mantle cpx, and ii) the rheology of diopside single crystals was thoroughly investigated at room P in the early 1990's, which gives 1-atm reference data for comparison with our high-pressure data. The present steady-state deformation experiments were carried out in a Deformation-DIA

apparatus (D-DIA) coupled with X-ray synchrotron radiation. This high-pressure equipment (see Durham et al., 2002, and Wang et al., 2003) allows measurement *in situ* of the applied stress (see Li et al., 2004; Burnley and Zhang, 2008) and resulting specimen strain rates (Raterron et al., 2007, and 2009).

2. Samples and deformation experiments

2.1 Starting material

Eleven cylindrical specimens - about 1.4 mm in diameter and up to ~2 mm in length - were cored in natural centimeter-sized diopside crystals, and polished on both ends. The starting crystals were of gem-quality, dark green and transparent, and contained no detectable defect at the binocular microscope scale. Their formula was determined either by electron microprobe or by energy dispersive spectroscopy (EDS) in the transmission electron microscope. It varies slightly (fractions of at.%) from one crystal to the next, with an average formula:

$$Ca_{0.960}Na_{0.024}Mg_{0.947}Fe_{0.043}Cr_{0.015}Ti_{0.002}Al_{0.008}Mn_{0.004}Ni_{0.007}Si_{1.994}O_6$$

2.2 Crystal orientations and active slip systems

In the pyroxene structure (see Cameron and Papike, 1981), dislocation lines cannot cut through the $(SiO_3)_\infty$ chains because of the strong Si-O-Si bound. In the diopside monoclinic structure (C2/c space group), this allows four possible glide planes: (100) and (010) planes, and two duplex planes {110}. According to previous experimental studies, twinning in (100) and (001) is in diopside a major deformation process at low temperature - typically lower than 800°C, e.g., Avé Lallemant (1978). At temperature higher than 1000°C, diopside plastic deformation is dominated by the activation of duplex ½<110>$\{1\bar{1}0\}$ dislocation slip systems (e.g., Raterron et al., 1994), with Burgers' vector ($\boldsymbol{b_r}$) 0.66 nm in length. These systems are followed in

activity by [001]{110} then by [001](100), both with $\|\boldsymbol{b_r}\|$ = 0.52 nm, while [100](010) and [010](100) slip systems remain marginal because of their large Burgers vectors (0.97 and 0.89 nm, respectively).

In order to test the activities of diopside dislocation slip systems, specimens were cut in three crystallographic orientations, which were verified by transmission electron microscopy (TEM). Cylinders were cut with their long axes within 5 degrees of the chosen orientations parallel to [010], [110] and [225] directions, corresponding to the orientations respectively labelled [2], [3], and [4] by previous authors (Raterron and Jaoul, 1991; Jaoul and Raterron, 1994; Raterron et al., 1994). Five specimens were cut in orientation [2], , which allows the duplex ½<110>{1 $\bar{1}$ 0} systems with a maximum Schmid factor $S \sim 0.5$ (Table 1). Three other specimens were cut in orientation [3] which allows mostly both [100](010) and [010](100) systems (with $S \sim 0.5$). Finally three specimens were cut in orientation [4] in order to activate [001] glide in (100), (010) and {110} planes, with $0.3 \leq S \leq 0.5$ in all glide planes.

2.3 Deformation apparatus and deformation protocols

Specimens were deformed in between two alumina pistons, in compression along their axis - at P ranging from 3.8 to 8.8 GPa, T within 1100°-1400°C, and at σ ranging from 210 to 1660 MPa (details below) - in the D-DIA on the X17-B2 beam line of the National Synchrotron Light Source (NSLS, Upton, NY, USA). We used boron-epoxy cubic pressure media and, to compress the cells, tungsten carbide anvils opaque to the X rays together with 1 or 2 transparent sintered-diamond anvils to allow back lateral (horizontal) diffraction. For the deformation cell, we used a similar design as that reported in Raterron et al. (2009); within the 6.15-mm D-DIA cell, temperature was generated using a vertical graphite furnace separated from the boron epoxy cube by an

alumina sleeve, and from the sample by a BN sleeve. Temperature was measured with two horizontal W3%Re-W25%Re thermocouples which junctions placed next to the vertical compression column in the middle of the cell. The uncertainty on temperature, mostly due to *T* gradients within the cell (no pressure correction), has been previously measured in the center of similar cells to less than 20 K/mm. Given the size of our specimens and other possible sources of errors, such as the effect of *P* on thermocouple emf and/or the distance between thermocouple and sample, we estimate run *T* uncertainty to ±100°C in a deformed cell; this large uncertainty also results from a power vs. temperature relationship which evolves with the cell strain, promoting significant deviations from calibration curves at large strain.

Two types of experiments were conducted: single-crystal experiments, where one single crystal is loaded (Figure 1.a), and bi-crystal experiments (Figure 1.b) where two crystals of different orientations are loaded in a given cell. This latter geometry, introduced by Raterron et al. (2007), ensures that both crystals experience the same stress field during deformation. It allows direct comparison of crystal deformations (i.e., of dislocation slip system activities) at identical *T*, *P*, and σ conditions, with no need of precise knowledge of the applied stress. Along the compression column, we used porous-alumina pistons in order to accommodate cold compression deformation (piston cataclastic compaction) with as little damage as possible on specimen(s) and calibrants (details below). At pressure and temperature, porous alumina becomes dense, hard sintered, which ensures the piston strength during deformation. Re foils were used to mark samples ends on the radiographs (Figure 1) and allow *in situ* measurement of sample strain and strain rate (details below).

Experimental run conditions and resulting specimen strains and strain rates are reported in Table 2, where they are regrouped by crystal orientations for a total of 33

steady state conditions. Three of the 8 conducted experiments, runs Dio18, Dio21 and Dio24, were bi-crystal experiments with 2 diopside crystals of different orientations in each cell. The other 5 experiments (Dio06, Dio11, Dio12, Dio17, and Dio19) were single-crystal experiments. During all experiments, specimens were cold compressed to the desired pressure in typically 3 to 4 hours. T was then increased in 30 min to 1 hour to 1000°C or more. Stress free and constant P and T conditions were maintained until diffraction patterns arising from the polycristalline stress calibrants within the cell (olivine, forsterite, spinel and/or alumina, see below) showed no evidence of stress remaining from cold compression, i.e., no peak broadening and similar spectra on all EDS detectors. Both inner (vertical) rams of the D-DIA were then moved forward at constant rates to deform the cell assembly, which usually translated into specimen steady state deformation. All of the reported data in Table 2 correspond to steady state deformation condition, i.e., constant stress and specimen strain rate. Each steady state condition corresponds, for all but 5 of the 33 experimental points, to a specimen strain of about 3 % (and up to 10 %). Strains < 2 % are only obtained when one crystal in the hard orientation [3] is deformed together with a soft orientation-[2] crystal (bi-crystal experiments). This was the case during runs Dio21 and Dio24 (Table 2), where crystals in orientation-[2] and the cells achieved large strains before the experiments were stopped. During all experiments, the applied stress σ and resulting specimen strain (ε) and strain rate ($\dot{\varepsilon}$), as well as pressure, were measured in situ by X-ray radiography and diffraction (see next section). Specimens were quenched (temperature dropped quickly) at the end of the runs, by cutting off the furnace power. Pressure was then decreased to room P within 2 to 3 hours. To preserve specimen deformation microstructures during decompression, specimen length was monitored by radiography and maintained constant by adjusting D-DIA inner-ram decompression rate manually. This latter

adjustment was, however, not very accurate and specimens often achieved some strain (typically 0.5 to 1 % strain) during cold decompression.

2.4 In situ stress and strain rate measurements

P, σ, and $\dot{\varepsilon}$ were monitored by time-resolved x-ray diffraction and radiography. These techniques allow *in situ* measurement of P and stress applied on specimens, and resulting specimen strain rates. Pressure and applied stress were measured from the quantification of x-ray peak shifts in diffraction patterns arising from stress calibrants: polycrystalline olivine (San Carlos olivine or pure forsterite Fo100) and spinel pellets placed in the compression column, and/or the piston polycrystalline alumina. Stress calibrants were separated from the sample(s) by Re foils (Figure 1). Except for the alumina pistons and spinel pellets, calibrants were loose powders at the beginning of the runs and were sintered at pressure and temperature. Pressure was deduced from calibrant unit-cell volumes using the corresponding equations of state (for San Carlos olivine and pure forsterite: Isaak (1992), Zha et al. (1996); for spinel: Askarpour et al. (1993), Anderson and Isaak (1995), Kruger et al.(1997); and for alumina: Anderson et al.(1992)), while stress $\sigma = \sigma_1 - \sigma_3$ was deduced from differences in the d-spacing characterizing lattice planes in different orientations with respect to the principal stress σ_1 (Li et al., 2004; see also Singh et al., 1998). Stress uncertainty using these techniques is fairly large, since it depends on the mechanical response of individual grains to the applied stress (Burnley et Zhang, 2008; Merkel et al., 2009), as well as the accuracy of - d-spacing measurement - i.e., on the position of X-ray diffraction peak maxima and shifting toward higher energy on compression (smaller d-spacing) - which in turn depends on several experimental factors (see Raterron et al., 2007). For this calculation, we assumed that σ_1 was homogeneous along the vertical compression column, and that the (horizontal) σ_3 was constant throughout the BN sleeve surrounding the samples.

This was often verified by the consistency, within uncertainties, in stress values measured using different calibrants. In some cases however, mostly at temperature of 1100°C, stress values obtained from different materials gave inconsistent results. This discrepancy may be due to several factors: i) at 1100° C, parts of the assembly such as the alumina pistons may not fully relax, leading to pressure and stress gradients within the cell; ii) stress-calibrant diameter depends on material responses to cold compression - the softer, the larger diameter, i.e. the more materials out of the compression column - which may result in underestimating the applied stress. Other sources of discrepancy includes: iii) different uncertainties on different equation-of-state parameters and elastic-constants used to process the data; iv) stress-calibrant grain growth, leading to offset diffraction peak positions; v) diffraction peaks from cell materials (BN, Re foils, etc.) superimposed on stress calibrant peaks; iv) Re strain markers partly shield the vertical EDS detectors from diffracted x-rays, etc.

Specimen plastic strain was measured on time-resolved X-ray radiographs collected on an x-ray fluorescent YAG crystal. Radiographs were recorded after magnification on a CCD camera. Sample and calibrant end positions appear as black lines on the radiographs (e.g., Raterron et al., 2007). These lines result from X-ray absorption by 25-µm thick metal-foils (strain markers: here Re foils). They allow measurement of specimen length $l(t)$ as a function of time, from which specimen strain and strain rate can be deduced. Specimen strain as a function of time $\varepsilon(t)$ was deduced from l(t) using the relationship: $\varepsilon(t) = \ln l_o/l(t)$ (here in compression $\varepsilon(t) \geq 0$), where l_o is the initial length of the specimen at given conditions. Steady-state strain rates ($\dot{\varepsilon}$) and their uncertainties were then deduced from straight slopes observed over more than typically 1% strain on $\varepsilon(t)$ versus time plots, all other parameters (P, T, and σ) being constant.

2.5 Run oxygen fugacity (fO_2) and silica activity (a_{SiO_2})

Diopside plastic properties depend slightly on oxygen fugacity, with an fO_2 exponent $m \sim -0.2$ in single-crystal rheological laws (Jaoul and Raterron, 1994). fO_2 was not controlled during our runs, although the Re-foils used as strain markers stayed in contact with diopside specimens during the runs. Re metal was still present in the run products, and no obvious sign of diopside reduction or oxidation (change of crystal color, intracrystalline precipitates) was detected by optical microscopy or TEM. This suggests that specimens stayed in their fO_2 stability field during the run. The pressure of either olivine or forsterite (used as stress calibrant in every cell) has implications for silica activity. Contact with the diopside specimens was maintained on the sides of the Re foils. Silica-rich precipitates were not observed within run products which shows that diopside early partial melting (EPM, e.g., Doukhan et al., 1993; Raterron et al., 1995) did not occur during our experiments.

2.6 Sample water contents

Diopside crystals can host significant amounts of water (e.g. Bell and Rossman, 1992). One can distinguish, however, between the hydroxyl (OH^-) groups part of amphibole lamellae present as inclusions within diopside bulk, from the OH^- present in diopside solid solution as protons (H^+) linked to structural oxygen. These two types of hydroxyls do not have the same effects on crystal rheology, since amphibole (not structural) hydroxyls do not affect diopside dislocation activities while H^+ defects within diopside may significantly affect diopside rheology (see Chen et al., 2006). It is, however, not trivial to separate the contribution of each type of hydroxyl group in unpolarized Fourier transformed infrared (FTIR) spectra. In the following, we assume that all hydroxyls detected by FTIR in the diopside crystals we investigated are related

233 to structural H^+ defect concentration, since no amphibole inclusions were observed in
234 the crystals, either optically or by TEM.

235 I.R. spectra were obtained using a PerkinElmer 2000 spectrometer fitted with a
236 MCT/B nitrogen-cooled detector attached to a microscope. An unpolarized beam was
237 focused on several regions of each ~ 0.3 to 0.5-mm thick double-polished section cut
238 from the starting crystals or the retrieved deformed specimens. Residues of the epoxy
239 used to preserve the run products during section preparation resulted in a wide band in
240 the middle of the spectra, which was subtracted in order to reveal the OH-bands
241 observable in the range 3200 and 3800 cm^{-1}. The absorbance normalized to 1-cm
242 sample thickness was obtained by integrating four OH-bands centered at 3647, 3530,
243 3435 and 3355 cm^{-1}, using Bell et al.'s (1995) calibration. We are aware that Bell et al
244 (1995) calibration is given for polarized IR measurements, while we used unpolarized
245 IR. Unfortunately there is no theoretical basis for a relationship between polarized and
246 unpolarized measurements. In the case of olivine, Bell et al. (2003) showed that
247 unpolarized IR measurements may underestimate hydroxyl contents by a factor ranging
248 from 1.5 to 3.5, depending on the assumed orientation factor. On this basis, we
249 systematically multiply by 3 the absorbance we measured in our samples before
250 calculating the resulting water contents. Because of this rough correction, the water
251 contents reported here may be overestimated and the relative uncertainty is large, on the
252 order of 50%. The water contents measured in starting material and run products using
253 the method described above are reported in Table 3.3. Results
254

3.2 Run product microstructures

Quenched run products were investigated by optical microscopy and TEM. The corresponding observations will be reported in details in a companion paper ("Deformation of diopside single crystals at mantle pressure 2: TEM characterization of dislocation microstructures"); we report here a short summary of the observed microstructures.

Petrographic sections ~ 30-μm thick were prepared from the retrieved specimens. Sections for TEM were ion thinned to electron transparency with a 5-kV argon beam, then carbon coated and investigated with a Philips CM30 electron microscope operating at 300 kV. TEM investigation revealed the dislocation slip systems expected to be active in each crystal orientation – i.e., in orientation [2] the duplex ½<110>$\{1\,\bar{1}\,0\}$ systems; in orientation [3] both [100](010) and [010](100) systems; in orientation [4] glide of [001] dislocation in {110}, (100), and (010) planes. TEM observations also show that, although ½<110> and [001] were as expected responsible for most specimen strain in orientation [2] and [4], respectively, these systems contribute to some extent to the deformation of all specimens. In order to quantify this effect, their contributions to specimen strain were calculated from geometrical considerations and the observed dislocation densities. We estimate that ½<110> dislocation glide contributes to less than 7% and 14% of the strain of specimen in orientation [4] and [3], respectively, while glide of [001] dislocation in (100), (010) and {110} planes contributes to 20% and 8% of the strain of specimens oriented along [2] and [3], respectively.

TEM observations also reveal twin lamellae which in most sample are likely the result of cold decompression, although high-temperature twinning may have also

278 occurred in sample subjected to high stress levels (typically > 1 GPa) at high
279 temperature.

280 ***3.3 High-P rheological data analysis and results***

281 *Effect of P on ½<110> dislocation glide*

282 In order to quantify the effect of *P* on the activity of ½<110>{1 $\bar{1}$ 0} slip systems,
283 orientation-[2] specimen rheological data were fitted to a rheological law. A general
284 creep power law for an Fe-bearing silicate reads:

285 $$\dot{\varepsilon} = A\sigma^n fO_2^m \exp -\frac{E^* + PV^*}{RT} \qquad (1),$$

286 where *A*, *n*, *m* are constants, *R* is the gas constant, *E** is the activation energy, and *V** is
287 the activation volume which quantifies the effect of *P* on crystal high-*T* rheology. Since
288 diopside rheology does not strongly depend on fO_2 and specimens stayed in their fO_2
289 stability field during our experiments (see section 2), we omit the fO_2 term in Equation
290 (1) which leads to the expression:

291 $$\dot{\varepsilon} = A\sigma^n \exp -\frac{E^* + PV^*}{RT} \qquad (2)$$

292 During our experiments, *P* and *T* were known to within ± 0.5 GPa and ± 100°C,
293 respectively. Yet, the large uncertainty affecting σ values (typically > 30 MPa) prevents
294 the accurate determination of the stress exponent *n* in Equation (2) from the high-*P* data
295 alone, i.e. the full determination of specimen rheological laws. The large stress
296 uncertainty which affects only high-*P* data, addressed in details by Burnley and Zhang
297 (2008), lead Raterron et al. (2009) to combine room-*P* and high-*P* data to constrained
298 olivine rheological laws. In the following, we combine also our high-*P* data with the
299 room-*P* deformation data reported by Raterron and Jaoul (1991). These authors carried
300 out high-temperature creep experiments on diopside single crystals cut in orientation [2]
301 and of comparable composition to that of our specimens. Raterron and Jaoul's

experiments are thus similar to our experiments in all respects, but the applied P. The rheological laws they deduced from the data collected below 1130°C were unaffected by diopside EPM (see section 2) and are thus representative of equilibrated orientation-[2] crystal deformed at room P. At room pressure (P=0) Equation (2) becomes:

$$\dot{\varepsilon} = A\sigma^n \exp - \frac{E^*}{RT} \qquad (3).$$

Hence, high-P strain rates $\dot{\varepsilon}(P,T,\sigma)$ can be deduced from room-P strain rates $\dot{\varepsilon}(0,T,\sigma)$ by combining Equations (2) and (3):

$$\dot{\varepsilon}(P,T,\sigma) = \dot{\varepsilon}(0,T,\sigma) \times \exp - \frac{PV^*}{RT} \qquad (4).$$

At given T-σ conditions, values of V^* can be obtained from the slopes on $\ln(\dot{\varepsilon})$ versus ($-P/RT$) plots. Complete rheological laws taking into account the effect of P can thus be written using Equation (4), by coupling high-P data with well established room-P rheological laws as expressed in Equation (3).

Figure 2.a shows $\log_{10}(\dot{\varepsilon})$ versus ($-P/RT$) plots for crystals in orientation [2], as obtained from Table 2 data points coupled with room-P data points which were calculated using Raterron et al.'s (1991) rheological law. Error rectangles around high-P experimental points were calculated taking into account experimental uncertainties on P, T, and $\dot{\varepsilon}$, as reported in Table 2. Stress uncertainties were taken into account when calculating room-P strain rates: each high-P point, thus, corresponds to 2 room-P points (same symbol on Figure 2.a) which were plotted using either the minimum stress (open symbol) or the maximum stress (full symbol) as deduced from the stress values and uncertainties reported in Table 2. A maximum slope (solid line) and a minimum slope (dashed line) can thus be obtained for each high-P experimental point. These two slopes correspond to, respectively, maximum and minimum V^* values, and are constrained by i) the size of the P-T-$\dot{\varepsilon}$ uncertainty rectangle around each high-P point, and ii) the two calculated room-P strain rates corresponding to each high-P point. Indeed, room-P strain rates are calculated using the room-P rheological law as previously reported for crystal in orientation [2], with the high-P experimental T and

using either a minimum stress value (average stress minus its uncertainty) or a maximum stress value (average stress plus its uncertainty) as deduced from each high-*P* stress measurement. This method allows taking into account all sources of uncertainties, i.e. uncertainties on *P*, *T*, σ and $\dot{\varepsilon}$, when determining *V** values for crystal in orientation [2] as reported in Table 4.

From equivalent slopes obtained from ln($\dot{\varepsilon}$) vs. (*-P/RT*) plots, we deduced the maximum V^*_{max} and minimum V^*_{min} values compatible with each high-*P* point, reported in Table 4. Finally, taking into account uncertainties on experimental values $V_i^* = (V_i^*{}_{\max} + V_i^*{}_{\min})/2$, i.e., applying to each of them a weight $\omega_i = 1/(\delta V_i^*)^2$ where δV_i^* is the uncertainty $(V_i^*{}_{\max} - V_i^*{}_{\min})/2$, and using the general weighted mean value formula:

$$V^* = \frac{\sum_i \omega_i \times V_i^*}{\sum_i \omega_i} \qquad (5),$$

we obtained the mean value *V** = 17 ± 6 cm^3/mol for the orientation-[2] crystal rheological law (Equation 2). This *V** value completes the set parameters obtained at room-*P* by Raterron and Jaoul (1991), and leads to the complete set of parameters reported in Table 5. The large activation volume obtained here for crystals in orientation [2] shows that *P* significantly inhibits glide of ½<110> dislocations in {110} planes.

Figure 2.b shows $\log_{10}(\dot{\varepsilon})$ versus $(-1/RT)$ for crystal in orientation [2], as obtained from Table 2 data points corrected to nominal *P* = 6 GPa and σ = 300 MPa using the *V** and *n* values reported in Table 5. Error rectangles around the experimental points show uncertainties on experimental *T* and $\dot{\varepsilon}$, taking into account the uncertainties in σ. The plain line on Figure 2.b is a plot of orientation-[2] rheological law using Table 5 parameters in Equation (2). The dashed line was obtained with the *V** and *n* values reported in Table 5, fitting the experimental points (least square regression) to values for the pre-exponential factor *A* and the activation energy *E** in Equation (2). Figure

2.b shows that, although Table 4 parameters - with A, n, and E^* parameters obtained at room-P - account well for our high-P data, a fit through the high-P data alone leads to the higher activation energy $E^* \sim 702$ kJ/mol (instead of 442 kJ/mol at room P). Such an increase with pressure in the apparent activation energy E^* may result from a change with pressure in the mechanism for ½<110> dislocation glide. Further investigation is however needed to confirm this preliminary result.

½<110> glide activity vs. [100], [010] and [001] glide activities

Room-P rheological data for crystals in orientations [3] and [4] are too sparse (see Raterron and Jaoul, 1991, and Raterron et al., 1994) to apply the analytical method described above for orientation-[2] crystals. Bi-crystal experiments however, such as runs Dio18, Dio21 and Dio24, are designed to compare slip-system activities by comparing the strain rates of crystals in different orientations with respect to principal stress directions.

Figure 3.a shows specimen strain (ε) versus time during run Dio18, where one orientation-[2] crystal and one orientation-[4] crystal were loaded on top of each other in the assembly compression column (Figure 1.b). Both crystals experienced identical P-T-σ path during the run. Their resulting strains and strain rates are comparable - often identical within uncertainties - which shows that the high-T activities of the duplex ½<110>{$1\bar{1}0$} systems (orientation [2]) and that of [001] glide in and {110}, (100), and to a lesser extent (010) (orientation [4]), are comparable at mantle pressure ($6 < P <$ 9 GPa). This differs from observations at room P, which show that ½<110>{$1\bar{1}0$}systems dominate diopside deformation at high temperature (Raterron et al., 1994). This difference in the relative activities of ½<110> and [001] slips at room P and high P suggests that pressure inhibits ½<110> glide more than [001] glide. This should translates into a lower activation volume V^* in the rheological law (Equation 2) describing orientation-[4] crystal plasticity than that obtained for crystals in orientation [2] ($V^* \sim 17$ cm^3/mol), although further investigation is needed to establish this point.

Runs Dio21 and Dio24 (bi-crystal experiments) were designed to compare the activities of ½<110>{1 $\bar{1}$ 0} slip systems (orientation [2]) with activities of [100](010) and [010](100) systems activated together (orientation [3]). Figure 3.b shows specimen ε versus time during run Dio21. During this run, the crystal in orientation [2] deformed at strain rates 5 to 8 times higher than that of the crystal in orientation [3]. This shows that ½<110>{1 $\bar{1}$ 0} activity dominates over those of [100](010) and [010](100) at mantle pressures ($7 < P \leq 8$ GPa, Table 2 and 3). Results from run Dio24, where orientation-[2] crystal deformed more than twice as fast as orientation-[3] crystal, confirm this observation. A similar observation was made for room-*P* experiments, in which ½<110>{1 $\bar{1}$ 0} systems dominate deformation over [100](010) and [010](100) systems (Raterron et al., 1994). Both [100] and [010] dislocations have longer Burgers vectors ($\boldsymbol{b_r}$, respectively 0.97 and 0.87 nm long) than that of ½<110> dislocation (0.66 nm long), which increases the energy involved in dislocation glide by 2 (roughly $\propto \boldsymbol{b_r}^2$).

We conclude that ½<110>{1 $\bar{1}$ 0} slip systems and [001] glide in {110}, (100), and to a lesser extend (010), have comparable activities at high *P* and *T*. These systems largely dominate diopside deformation over [100](010) and [010](100) systems at mantle *P* and *T* conditions.

4. Discussion and geological implications

An important result of the present study is the quantification of the effect of *P* on ½<110>{1 $\bar{1}$ 0} slip system activity, which are dominant systems of diopside at room *P* and temperatures above 1000°C. Increasing pressure inhibits ½<110> glide, which translates into the activation volume V^*=17±6 cm^3/mol (Equation (2)) for crystals in orientation [2]. This shows that orientation-[2] crystals significantly harden with pressure. Diopside viscosity, thus, significantly increases with *P* (e.g., Figure 2.a). Assuming this property extrapolates to all mantle cpx, one can expect cpx to be much

stronger in the deep upper mantle - leading to reductions in strain rate by several orders on magnitude- than expected from room-*P* rheological laws. In this context, the complete rheological law reported here for crystals in orientation [2] (Table 2) provides a first clue to quantify cpx viscosity at mantle conditions.

TEM investigation of the run products (see companion article for details) shows that glide of ½<110> dislocations dominates deformation of orientation-[2] crystals. This suggests that the V^* value mostly results from an increasing lattice friction with *P* for ½<110> dislocations glide in {110} planes. This interpretation, however, cannot be definitive without proper modeling of ½<110> dislocation core and elastic properties. Indeed, empirical rheological laws such as Equation (2) account for differential stress and pressure as two independent variables. In fact, both σ and *P* are partial expressions of the stress tensor and their respective effects on crystal plasticity cannot be easily separated. This is particularly true in the case of dislocation creep, where crystal deformation results from dislocation mobility which strongly depends on their core structures. According to computational studies, dislocation cores are complex and extended in silicates, likely in several directions (e.g., Walker et al., 2005; Carrez et al., 2008), which makes them sensitive to both σ and *P*. This was recently modeled in the case of forsterite dislocations (Durinck et al., 2005; Durinck etal., 2007) which provided the theoretical background to explain the inhibition effect of *P* on olivine [100](010) slip system (Raterron et al., 2007; Raterron et al., 2009). Similar modeling is thus required to explain the inhibition effect of *P* on diopside ½<110>$\{1\,\bar{1}\,0\}$ slip systems observed here.

Another important result is that both ½<110> and [001] glides have comparable activities at mantle *P* and *T*. This observation differs from room-*P* observations (Raterron et al., 1994), which show that ½<110> glide is dominant at high temperature.

433 It is, however, consistent with the recent experimental study of omphacite rheology at 3
434 GPa reported by Zhang et al. (2006). These authors conclude that ½<110>{1 $\bar{1}$ 0},
435 [001]{110} and [001](100) slip systems dominate deformation at high-*T*. Our result is
436 also consistent with cpx lattice preferred orientations (LPOs) observed in naturally
437 deformed eclogites from various origins (The Alpes, Norway, Spain, Mali, China, etc.).
438 Omphacite and augite LPOs in deformed eclogites have been extensively studied over
439 the past 25 years (e.g., Van Roermund et Boland, 1981; Van Roermund, 1983; Buatier
440 et al., 1991; Skrotzki, 1994; Godard et Van Roermund, 1995; Bascou et al, 2001,
441 Brenker et al., 2002). In nature, cpx develop marked LPOs characterized by a strong
442 concentration of [001]-axes sub-parallel to the lineation and of (010)-poles roughly
443 normal to the foliation. Such LPOs form in relation with the deformation of eclogites
444 through dislocation creep, as revealed by TEM observations of naturally deformed cpx
445 grains. The LPOs are explained by self-consistent visco-plastic (VPSC) modeling of
446 cpx aggregate deformation (Bascou et al, 2001; Bascou et al., 2002). VPSC models
447 show, in the case of omphacite, that such LPOs can develop by the dominant activity of
448 ½<110>{1 $\bar{1}$ 0}, [001] {110} and [001] (100) dislocation slip systems, a result in
449 excellent agreement with the results reported here for diopside crystals deformed at
450 mantle *P* and *T*.

451

452 **References**

453 Anderson, O.L., and Isaak, D.G., 1995. Elastic constants of mantle minerals at high
454 temperature. In: T.J. Ahrens (Editor) Mineral Physics and Crystallography: a
455 handbook of physical constants, Am. Geophys. Union: 64–97.
456 Anderson, O.L., Isaak, D., and Oda, H., 1992. High-temperature elastic constant data on
457 minerals relevant to geophysics. Rev. Geophys., 30: 57-90.
458 Askarpour, V., Manghnani, H., Fassbender, S., and Yoneda, A., 1993. Elasticity of
459 single-crystal $MgAl_2O_4$ spinel up to 1273 K by Brillouin spectroscopy. Phys.
460 Chem. Miner., 19: 511-519.
461 Avé Lallemant, H.G., 1978. Experimental deformation of diopside and websterite.
462 Tectonophysics, 48: 1-27.
463 Bascou, J., Barruol, G. Vauchez, A., Mainprice, D., and Egydio-Silva, M., 2001. EBSD-
464 measured lattice-prefered orientations and seismic properties of eclogites.
465 Tectonophysics, 342: 61-80.
466 Bascou, J., Tommasi, A., and Mainprice, D., 2002. Plastic deformation and
467 development of clinopyroxene lattice preferred orientations in eclogites. J. Struct.
468 Geol., 24: 1357-1368.
469 Bell, D., and Rossman, G., 1992. Water in Earth's mantle: the role of Nominally
470 Anhydrous Minerals. Science, 255: 1391-1397.Bell, D., Ihinger, P., and Rossman, G.,
471 1995. Quantitative analysis of trace OH in garnet and pyroxenes. Am. Mineral., 80:
472 465-474.
473 Bell, D.R., Rossman, G.R., Maldener, J., Endisch, D., Rauch, F., 2003. Hydroxide in
474 olivine: a quantitative determination of the absolute amount and calibration of the
475 IR spectrum. J. of Geophys. Res., 108 (B2): 2105, doi:10.1029/2001JB000679.
476 Boland, J.N., and Tullis, T.E., 1986. Deformation behaviour of wet and dry
477 clinopyroxenite in the brittle to ductile transition region. In: B.E. Hobbs and H.C.
478 Heard (Editors). Mineral and Rock Deformation: Laboratory Studies. Am.
479 Geophys. Union, Geophys. Monogr., 36: 35-49.
480 Brenker, F., Prior, D., and Müller, W., 2002. Cation ordering in omphacite and effect on
481 deformation mechanism and lattice preferred orientation (LPO). J. Struct. Geol.,
482 24: 1991-2005.

483 Buatier, M., Van Roermund, H., Drury, M., and Lardeaux, J., 1991. Deformation and
484 recrystallisation mechanisms in naturally deformed omphacites from the Sesia-
485 Lanzo zone; geophysical consequences. Tectonophysics, 195: 11-27.
486 Burnley, P., and Zhang, D. 2008. Interpreting in situ X-ray diffraction data from high
487 pressure deformation experiments using Elastic Plastic Self Consistent models: an
488 example using quartz. J. Phys. Condens. Matter, 20: 285201.
489 Bystricky, M., and Mackwell, S., 2001. Creep of dry clinopyroxene aggregates. J.
490 geophys. Res., 106: 13,444-13,454.
491 Cameron, M., and Papike, J.J., 1981. Structural and chemical variations in pyroxenes.
492 Am. Mineral., 66: 1-50.
493 Carrez, P., Walker, A.M., Metsue, A., and Cordier, P., 2008. Evidence from numerical
494 modelling for 3D spreading of [001] screw dislocations in Mg2SiO4 forsterite.
495 Phil. Mag., 88: 2477–2485.
496 Chen, S., Hiraga, T., and Kohlstedt, D., 2006. Water weakening of clinopyroxenes in
497 the dislocation creep regime. J. Geophys. Res., 111: B08203.
498 Dimanov, A., Lavie, M.P., Dresen, G., Ingrin, J., and Jaoul, O., 2003. Creep of
499 polycrystalline anorthite and diopside. J. Geophys. Res., 108(B1): 2061.
500 Doukhan, N., Doukhan, J.C., Ingrin, J., Jaoul, O., and Raterron, P., 1993. Early partial
501 melting in pyroxenes. Am. Mineral., 78: 1246-1256.
502 Durham, W. B, Weidner, D. J., Karato, S.-i., and Wang, Y., 2002. New developments in
503 deformation experiments at high pressure. In: S.-i. Karato and H.-R. Wenk
504 (Editors). Reviews in Mineralogy and Geochemistry: Plastic Deformation of
505 Minerals and Rocks. Miner. Soc. Am., 51: 21–49.
506 Durinck, J., Legris, A., and Cordier, P., 2005. Pressure sensitivity of forsterite slip
507 systems: first-principle calculations of generalised stacking faults. Phys. Chem.
508 Miner., 32: 646-654.
509 Durinck, J., Carrez, P., and Cordier, P., 2007. Application of the Peierls-Nabarro model
510 to dislocations in forsterite, Eur. J. Mineral., 19: 631-639.
511 Godard, G., and Van Roermund, L., 1995. Deformation-induced clinopyroxenes fabrics
512 from eclogites. J. Struct. Geol., 17(10): 1425-1443.
513 Green, D., and Ringwood, A., 1963. Mineral assemblages in a model mantle
514 composition. J. Geophys. Res., 68: 937-945.

515 Griggs, D.T., Turner, F.J., and Heard, H.C., 1960. Deformation of rocks at 500° to
516 800°C. In D. Griggs and J. Handin (Editors). Rock Deformation. Bull. Geol. Soc.
517 Am., 79, 39-104.
518 Ingrin, J., Doukhan, N., and Doukhan, J.C., 1991. High-temperature of diopside single
519 crystal 2: Transmission electron microscopy investigation of the defect
520 microstructures. J. Geophys. Res., 96: 14,287-14,297.
521 Ingrin, J., Doukhan, N., and Doukhan, J.C., 1992. Dislocation glide systems in diopside
522 single crystals deformed at 800-900°C. Eur. J. Mineral., 4: 1291-1302.
523 Isaak, D.G., 1992. High-temperature elasticity of iron-bearing olivines. J. Geophys.
524 Res. B: Solid Earth and Planets, 97(2): 1871–1885.
525 Jaoul, O., and Raterron, P., 1994. High-temperature deformation of diopside crystal, 3:
526 Influences of pO_2 and SiO_2 precipitation. J. Geophys. Res., 99: 9423-9439.
527 Kirby, S.H., and Kronenberg, A.K., 1984. Deformation of clinopyroxenite: evidence for
528 a transition in flow mechanisms and semibrittle behaviour. J. Geophys. Res., 89:
529 3177-3192.
530 Kollé, J.J., and Blacic, J.D., 1982. Deformation of single crystal clinopyroxenes 1:
531 Mechanical twinning in diopside and hedenbergite. J. Geophys. Res, 87: 4019-
532 4034.
533 Kollé, J.J., and Blacic, J.D., 1983. Deformation of single crystal clinopyroxenes, 2:
534 Dislocation-controlled flow processes in hédenbergite. J. Geophys. Res, 88: 2381-
535 2393.
536 Kruger, M.B., Nguyen, J.H., Caldwell, W., and Jeanloz, R., 1997. Equation of state of
537 $MgAl_2O_4$ spinel to 65 GPa. Phys. Rev. B, 56(1): 1-4.
538 Li, L., Weidner, D., Raterron, P., Chen, J., and Vaughan, M., 2004. Stress
539 measurements of deforming olivine at high pressure. Phys. Earth Planet. Inter.,
540 143: 357-367.
541 Mainprice, D., Barruol, G., and Ben Ismaïl, W., 2000. The seismic anisotropy of the
542 Earth's Mantle: From Single crystal to polycristal. In: S.-i. Karato, A. Forte, R.
543 Liebermann, G. Masters, L. Sixrude (Editors). Earth's deep interior: Mineral
544 Physics Tomography from Atomic Scale to the Global Scale. Am. Geophys.
545 Union, Geophys. Monogr. 117: 237-264.

546 Mauler, A., Bystricky, M., Kunze, K., and Mackwell, S., 2000. Microstructures and
547 lattice preferred orientations in experimentally deformed clinopyroxene
548 aggregates. J. Struct. Geol., 22: 1633-1648.
549 Merkel, S., Tomé, C., and Wenk, H.-R., 2009. A modeling analysis of the influence of
550 plasticity on high pressure deformation of hcp-Co, *Phys. Rev. B* 79, 064110.
551 Raleigh, C.B., and Talbot, J.L., 1967. Mechanical twinning in naturally and
552 experimentally deformed diopside. Am. J. Sci., 265: 151-165.
553 Raterron, P., and Jaoul, O., 1991. High-Temperature deformation of diopside single
554 crystal, 1: Mechanical data. J. Geophys. Res., 96: 14,277-14,286.
555 Raterron, P., Doukhan, N., Jaoul, O., and Doukhan, J.C., 1994. High temperature
556 deformation of diopside, IV: predominance of {110} glide above 1000°C. Phys.
557 Earth Planet. Int., 82: 209-222.
558 Raterron, P., Ingrin, J., Jaoul, O., Doukhan, J.C., and Elie, F., 1995. Early partial
559 melting of diopside under high-pressure. Phys. Earth Planet. Int., 89: 77-88.
560 Raterron, P., Chen, J., Li, L., Weidner, D., and Cordier, P., 2007: Pressure-induced slip-
561 system transition in forsterite: Single-Crystal rheological properties at mantle
562 pressure and temperature. Am. Mineral., 92: 1436-1445.
563 Raterron, P., Amiguet, E., Chen, J., Li, L., and Cordier, P., 2009. Experimental
564 deformation of olivine single crystals at mantle pressures and temperatures, Phys.
565 Earth Planet. Interiors, 172: 74-83
566 Singh, A.K., Balasingh, C., Mao, H.-K., Hemley, R., and Shu, J., 1998. Analysis of
567 lattice strains measured under nonhydrostatic pressure. J. Appl. Phys., 83(12):
568 7567–7575.
569 Skrotzki, W., 1994. Defect structure and deformation mechanisms in naturally
570 deformed augite and enstatite. Tectonophysics 229: 43-68.
571 Van Roermund, H., and Boland, J., 1981. The dislocation substructures of naturally
572 deformed omphacites. Tectonophysics, **78**: 403-418.
573 Van Roermund, H., 1983. Petrofabrics and microstructures of omphacites in a high
574 temperature eclogite from the Swedish Caledonides. Bull. Minér., 106: 709-713.
575 Walker, A.M., Gale, J.D., Slater, B., and Wright, K., 2005. Atomic scale modelling of
576 the cores of dislocations in complex materials part 2: applications. Phys. Chem.
577 Chem. Phys., 7: 3235-3242.

578 Wang, Y., Durham, W.B., Getting, I.C., and Weidner, D.J., 2003. The Deformation
579 DIA: a new apparatus for high temperature triaxial deformation to pressure up to
580 15 GPa. Rev. Sci. Instrum., 74: 3002-3011.
581 Zha, C.-S., Duffy, T.S., Downs, R.T., Mao, H.-K., and Hemley, R.J., 1996, Sound
582 velocity and elasticity of single-crystal forsterite to 16 GPa. J. Geophys. Res. B:
583 Solid Earth Planets 101 (8): 17535–17545.
584 Zhang, J., Green, H.W., and Bozhilov, K., 2006. Rheology of omphacite at high
585 temperature and pressure and significance of its lattice preferred orientations.
586 Earth Planet. Sci. Lett., 246: 432-443.
587 Zhang, J., and Green, H.W., 2007. Experimental investigation of eclogite rheology and
588 its fabrics at high temperature and pressure. J. Metamorphic Geol., 25: 97-115.

589

590

591

592 **Acknowledgements:** The authors thank Liping Wang for his assistance at the NSLS
593 beamline X17-B2 (supported by the U.S. Department of Energy, contract # DE-
594 AC02_98CH10886 and COMPRES), as well as Andreas Kronenberg and an
595 anonymous reviewer for their comments and suggestiuons to improve the original
596 manuscript. This research was supported by the NSF Grant EAR-9909266,
597 EAR0135551, and EAR0229260, and the Centre National de la Recherche Scientifique
598 CNRS / INSU Grants "DyETI 2004" and "DyETI 2005", the CNRS "Programme
599 International de Collaboration Scientifique" (PICS project), as well as the French ANR
600 grant "Mantle Rheology" (# BLAN08-2_343541). The TEM national facility in Lille is
601 supported by the CNRS (INSU) and the Conseil Régional du Nord – Pas de Calais,
602 France.

603

604 **Table 1:** Schmid factors for potential slip systems

Slip systems	Orientation [2]	Orientation [3]	Orientation [4]
[001](100)	0	0.14	0.36
[001](010)	0	0.13	0.34
[001](110)	0	0.19	0.49
[001](1$\bar{1}$0)	0	0	0
[110](1$\bar{1}$0)	0.49	0	0
[1$\bar{1}$0](110)	0.49	0.09	0.07
[010](100)	0	0.48	0.30
[100](010)	0	0.5	0.20

605

606

607 **Table 2**. Experimental conditions and results for crystals in orientation [2], [3] and [4]

Run	Point #	Pressure (GPa)	Temperature (°C)	Stress (MPa)	Strain rate (10^{-6} s^{-1})	Total strain (%)
			orientation [2]			
Dio17	17-1	7.8 ± 0.4	1400	333 ± 74[a]	15.4 ± 1.5	5.0
1800µm	17-2	7.6 ± 0.4	1400	290 ± 100[a]	8.7 ± 1.5	3.2
	17-3	6.4 ± 0.6	1200	505 ± 100[a]	11.9 ± 1.6	5.0
Dio18	18-1	8.8 ± 0.1	1400	236 ± 100[ab]	14.2 ± 2.2	5.8
1070µm	18-2	7.9 ± 0.3	1400	210 ± 48[ab]	6.1 ± 1.7	3.4
	18-3	7.0 ± 0.2	1200	928 ± 35[ab]	16.3 ± 2.0	8.2
	18-4	6.9 ± 0.1	1200	864 ± 52[a]	7.1 ± 2.1	3.6
	18-5	6.4 ± 0.1	1200	499 ± 65[b]	7.1 ± 2.1	3.6
Dio19	19-1	7.5 ± 0.6	1300	500 ± 80[a]	18.9 ± 1.7	6.3
1700µm	19-2	6.9 ± 0.2	1300	373 ± 80[a]	9.0 ± 1.5	3.7
	19-3	7.3 ± 1.0	1100	1660 ± 140[ab]	31.0 ± 2.2	9.3
	19-4	6.3 ± 1.0	1100	1606 ± 230[ab]	10.2 ± 1.7	4.5
Dio21	21-1	8.0 ± 1.1	1400	282 ± 46[ab]	21.2 ± 1.5	6.5
1250µm	21-2	7.3 ± 0.8	1400	276 ± 75[ab]	12.5 ± 1.2	5.5
Dio24	24-1	8.0 ± 0.7	1300	354 ± 82[ab]	12.7 ± 1.1	5.6
1050m	24-2	8.2 ± 0.3	1300	252 ± 66[ab]	7.4 ± 1.0	4.3
			orientation [3]			
Dio06	6-1	8.3 ± 0.2	1200	1347 ± 200[ad]	28.5 ± 3.5	6.4
1970µm	6-2	8.1 ± 0.1	1200	975 ± 330[ad]	11.0 ± 2.2	4.2
Dio21	21-1	8.0 ± 1.1	1400	282 ± 46[a]	3.8 ± 1.4	1.2
1280µm	21-2	7.3 ± 0.8	1400	276 ± 75[b]	1.5 ± 1.0	0.7
Dio24	24-1	8.0 ± 0.7	1300	354 ± 82[ab]	4.4 ± 1.7	1.8
710µm	24-2	8.2 ± 0.3	1300	252 ± 66[ab]	3.2 ± 1.3	1.9
			orientation [4]			
Dio11	11-1	5.7 ± 0.2	1300	493 ± 150[c]	10.8 ± 2.0	2.6
1110µm	11-2	5.0 ± 0.2	1300	347 ± 160[c]	7.8 ± 1.3	2.9
	11-3	3.8 ± 1.7	1100	943 ± 220[ac]	4.6 ± 1.2	2.0
	11-4	4.5 ± 2.0	1100	1010 ± 220[ac]	37.5 ± 2.3	9.0
Dio12	12-1	7.7 ± 0.2	1400	213 ± 180[c]	14.5 ± 1.3	4.2
1380µm	12-2	8.5 ± 0.9	1400	349 ± 86a[c]	6.7 ± 1.0	3.5
	12-3	7.0 ± 0.1	1200	608 ± 280[c]	5.0 ± 1.2	3.6
	12-4	7.2 ± 0.1	1200	645 ± 170[c]	34.4 ± 1.6	10.1
Dio18	18-1	8.8 ± 0.1	1400	236 ± 100[ab]	11.8 ± 1.8	4.9
1220µm	18-2	7.9 ± 0.3	1400	210 ± 48[ab]	5.5 ± 1.4	3.0
	18-3	7.0 ± 0.2	1200	928 ± 35[ab]	23.7 ± 2.7	7.4
	18-4	6.9 ± 0.1	1200	864 ± 52[a]	7.1 ± 2.1	3.0
	18-5	6.4 ± 0.1	1200	499 ± 65[b]	7.1 ± 2.1	3.0

608 [a] *alumina σ sensor,* [b]*San Carlos olivine σ sensor;*[c] *Forsterite σ sensor*, [d] *Spinel σ sensor*

609

610 **Table 3:** Hydroxyl content in starting material and deformed samples

Sample	OH^- content ($H/10^6$ Si)
Starting material	8960
Dio19 (orientation [2])	1640
Dio11 and Dio18 (orientation [4])	2480
Dio24 (orientation [3])	3950

611

612 **Table 4:** V^* values obtained for crystal in orientation [2]

Run	Point #	V^*_{min} (cm^3/mol)	V^*_{max} (cm^3/mol)
Dio17	17-1	11	23
	17-2	9.1	24
	17-3	9.8	22
Dio18	18-1	4.4	18
	18-2	7.8	19
	18-3	16	26
	18-4	16	28
	18-5	11	28
Dio19	19-1	12	23
	19-2	11	24
	19-3	15	24
	19-4	17	32
Dio21	21-1	9.7	19
	21-2	9.6	23
Dio24	24-1	8.2	18
	24-2	1.1	18

613 V^*_{min} and V^*_{max}: respectively minimum and maximum V^* obtained
614 in ln(strain rate) versus $-P/RT$ plots, taking into account uncertainties
615 on P, T, σ, and fO_2. The weighted mean V^* value is obtained using
616 Equation (5).
617
618

619 **Table 5:** Equation (2) parameters for crystals in orientation [2]

Ln(A) †	n †	E^*(kJ/mol) †	V^*(cm^3/mol)
-7.8	6.46	442	17 ± 6

620 † from Raterron et al. (1991); A is in MPa^{-n}

621 **Figure 1**: schematic drawing of the compression column within a) the single-crystal
622 experiment cell and b) the bi-crystal experiment cell. Stress calibrants used here
623 include polycrystalline olivine, forsterite, spinel and alumina (see text and Table 2).

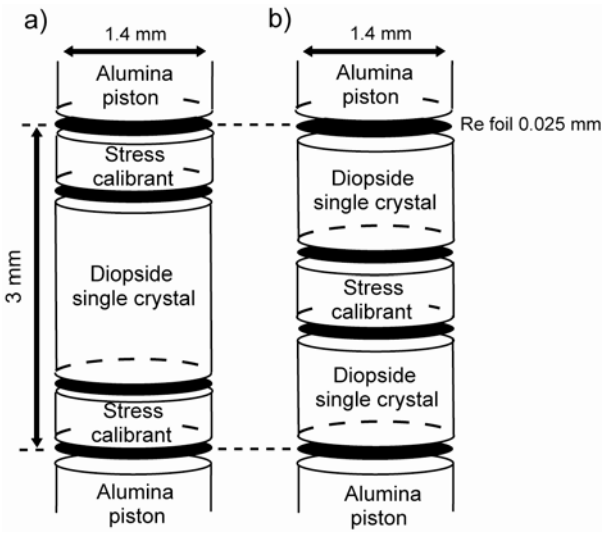

624

625

626

627

628

629

630

631 **Figure 2**: Orientation-[2] crystal high-*P* experimental points with corresponding
632 uncertainty rectangles. a) log(strain rate) vs. (P/RT) plot and corresponding *V** value in
633 Equation (2); at each high-*P* point correspond 2 room-*P* points, as obtained taking into
634 account σ uncertainty on high-*P* data and using Raterron and Jaoul's (1991) rheological
635 law. b) log(strain rate) vs. (1/RT) plot as extrapolated at the indicated *P*, σ conditions
636 using Table-5 parameters (indicated *V** value). See text for further explanation.

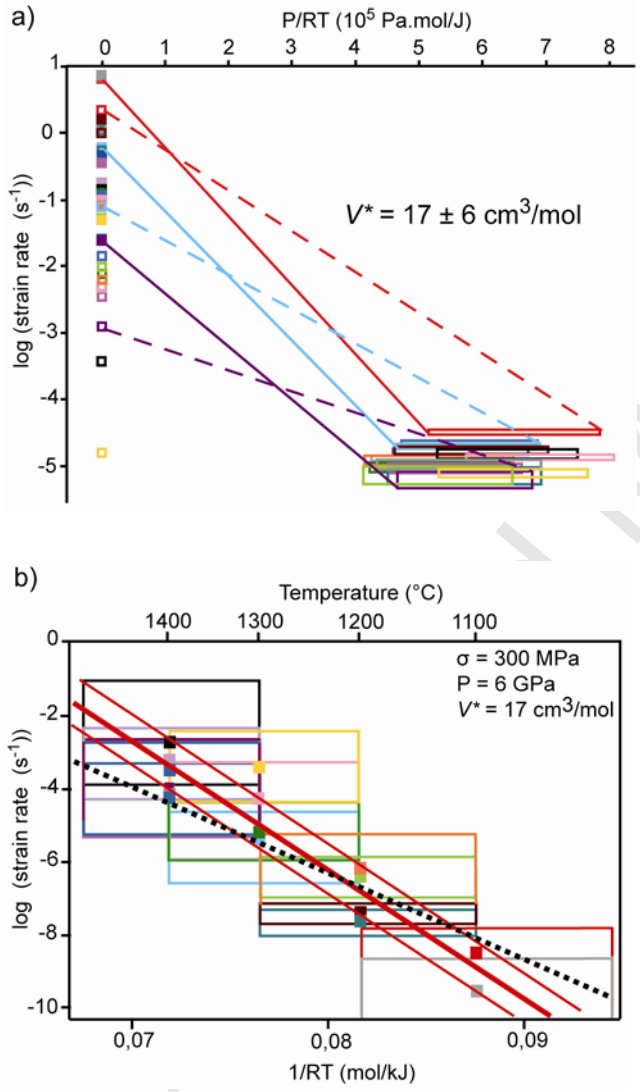

637

638

639

640

641 **Figure 3**: Specimen total strain (ε) versus time during bi-crystal runs a) Dio18 and b)
642 Dio21, showing the deformation of orientation-[2] crystals (black squares) with that of
643 crystals in orientation [4] and [3] (colored symbols), respectively. Vertical lines separate
644 different regimes of deformation at the indicated *P* and *T* conditions. The numbers next
645 to the deformation curves indicate corresponding steady-state strain rates (in 10^{-6} s^{-1}).
646 The corresponding stress values are listed in Table 2. See text for further information.

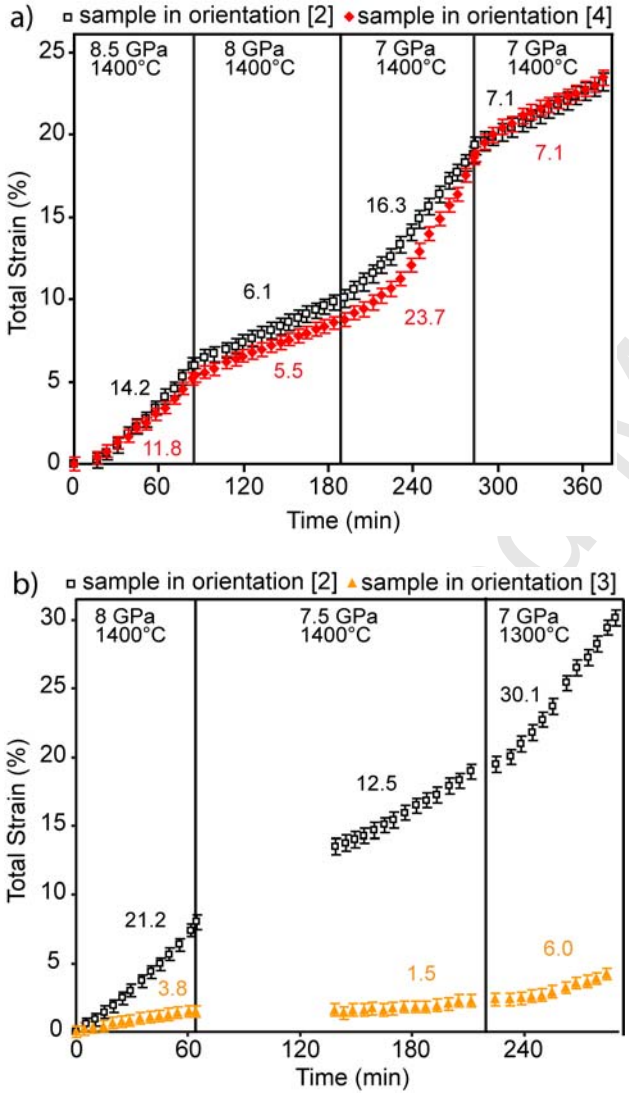

647